A MRI COMPATIBLE CONCENTRIC TUBE CONTINUUM ROBOT WITH PNEUMATIC ACTUATION

By

Diana C. Cardona

A thesis

Submitted to the Faculty of the

Graduate School of Vanderbilt University

partial fullfillment of the requirements

for the degree of

Master of Science

in

Mechanical Engineering

May, 2012

Nashville, Tennessee

Approved:

Robert J. Webster III

Thomas J. Withrow

Eric J. Barth

A papá y mamá,

por apoyarme en todos mis proyectos y animarme a volar alto.

Gracias por darme todo lo invisible a los ojos que me hace ser quien soy.

Acknowledgements

Abstract

The aim of this study is to develop a magnetic resonance imaging (MRI) compatible robot to enable image guided interventions to enhance accuracy and reduce invasiveness. MRI provides exquisite soft tissue images, and fluid power is an enabler of its use in surgery. Its advantages are not completely explored yet because traditional electromagnetic actuators fail or cause artifacts in intense magnetic fields and the space inside the bore is limited. In order to overcome these constraints, we are designing and developing a compact and MRI-compatible system with an active cannula, operated by pneumatic actuation. The active cannula uses precurved concentric tubes, and the ensemble changes shape as tubes extend and spin axially. The robot employs MRI-compatible pneumatic cylinders with the goal of eliminating the artifacts that can be created by other actuation technologies. The robot is designed to perform a MRI-guided ablation of the hippocampus for patients with severe epilepsy using a MRI-compatible ablator. This thesis describes the development of the robot including design and workflow considerations, mechanical design, MRI-compatibility evaluation, control evaluation and both benchtop and in-scanner accuracy studies.

Contents

List of Figures

Chapter 1

Introduction

1.1 Motivation and Related Work

Image guided surgery presents an advantage in procedures that require the surgeon to look at preoperative images to plan the intervention and it also allows less invasive procedures and therefore reduces risks to the patient. The use of Magnetic Resonance Imaging (MRI) as an imaging technology offers some advantages because of its high contrast between soft tissues, which makes it especially suitable for imaging the brain. Modern MRI is capable of providing images at high speed, which makes it possible to perform a surgery while getting real-time images. Despite all these advantages, MRI-guided surgery still presents challenges due to the restricted space available between the patient and the imager and the intense magnetic fields required.

1.1.1 Medical Motivation – Treatment of Epilepsy

Epilepsy is a neurological disorder, characterized by recurrent and unprovoked seizures [1], and one of the world's oldest recognized diseases [2]. Epilepsy is a significant public health problem. About 50 million people worldwide (2 million in the USA) have it, and it is usually controlled, but not cured, with medication. However, 15-40% of patients do not achieve seizure control with medication [3] and many have significant

side effects of medication even in the population who achieve good seizure control. Studies demonstrate that if initial anticonvulsant monotherapy is ineffective, trials of subsequent medications yield diminishing benefit. Failure to abolish seizures carries significant risks beyond the possible physical harm, and life disruption cause by unpredictable seizure events. Several studies have documented rates of Sudden Unexplained Death in Epilepsy of 7-17% of people with epilepsy [3]. This number may be significantly increased in patients who have failed medical therapy [4]. Additionally, the societal cost of these patients in medical care and lost productivity is staggering. Patients failing to obtain seizure control are estimated to have a 30-fold increase in lifetime disease cost [5]. Thus, an alternative therapy is strongly motivated by high incidence, the potential for surgical and medicinal complication reductions, improved quality of life for patients, and reduction in nationwide health care costs. For a better control of epilepsy, the seizure focus must be localized and surgical resection must be performed. Localization of the seizure focus can be achieved through the placement of intracranial electrodes or MRI imaging. There are 40 identified types of epilepsy, but one of the most common form is called Temporal Lobe Epilepsy or TLE, and in 70% of the cases its origin is located at the hippocampus [6]. Surgical resection of the hyppocampus (Figure 1.1) has held promise of significant rates of seizure freedom [7]. The efficacy of surgery in treating particular types of epilepsy has been demonstrated in randomized controlled trials and offers seizure-free rates approaching 70% [7–9]. The American Academy of Neurology has concluded that temporal lobectomy is effective in reducing seizures, improving quality of life, and reducing risk of long term mortality [10]. Despite the proven efficacy of surgery, undertreatment is greater than
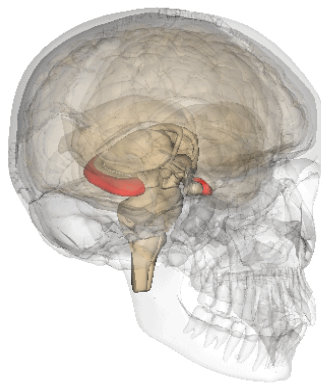
Figure 1.1: A Human skull with the hippocampus shown in red.

50% [11, 12], and it is estimated to be even higher in the USA [9]. The reason for such underutilization is believed to be inherent patient bias against surgical resection and the perceived morbidity of craniotomy [13].

1.1.2 Motivation for MRI Guided Intervention

Real-time feedback is preferable to traditional stereotactic surgery because it enables neurosurgeons to confirm that planning and execution errors have not occurred and to ultimately confirm the location of the therapeutic instrument tip with respect to anatomy. Potential sources of error in traditionally stereotaty include human error, software errors, and mechanical errors, as well as intraoperative brain shift. These factors all argue for real-time image feedback rather than pure traditional stereotaxy. It has been observed by Hall and Truwit that traditional stereotactic guidance can never be sufficient for highly accurate targeting, due to inability to account for inevitable brain shift that occurs once the cranium is opened and cerebrospinal fluid is lost. According to [14], the surface of the brain is deformed by up to 20mm after

craniotomy, and in deeper brain structures the principal direction of displacement does not always correspond with the direction of gravity. Therefore, computational algorithms that utilize limited intraoperative information (e.g., brain surface shift correction as in [15]) will not always accurately predict brain deformation at the clinical target site. Atlas-based models to predict brain shift [16] are a promising area of study, but cannot yet offer sufficient accuracy for our application. In contrast, intraoperative MRI can account for brain shift [17], and enable real-time in situ verification of proper plan execution. MRI is generally agreed to be the best imaging modality for soft tissue [18], [19], [20]. Since pre-operative MR images are the current basis of stereotactic procedures, performing these procedures with real-time MRI feedback is a natural progression from current stereotactic techniques. MRI also offers rapid high-resolution tissue imaging with slices at arbitrary orientations, and is able to monitor therapeutic agents, surgical tools, biomechanical tissue properties, and physiological function, which make MRI uniquely useful for guiding, monitoring and controlling a wide array of localized interventions [21], [22], [23]. Other advantages of MRI-guided intervention include excellent soft tissue discrimination, the ability to view the surgical site in three dimensions, and enhanced ability to avoid critical structures [17]. Direct MRI image guidance during stereotactic cannula delivery will enable visualization of insertion and confirmation of ablator tip placement accuracy with real-time treatment monitoring using MR thermal imaging (MRTI).

1.1.3   MRI-Compatible Robots

We propose a pneumatically-actuated steerable robotic approach for delivering the ablator tip to a desired target; a robot has the potential to be more accurate than humans, and can work within the confined space of a standard MRI machine. Surgery inside long bore, high-field magnets is facilitated by remote actuation [24], but presently available MRI compatible robots suffer from problems that include complexity, size, and kinematic limitations [25]. However, non-MRI compatible robots have been widely used for stereotaxy (see e.g. [26] among many others), and guidance using real-time image feedback during surgery has been made with commercially available systems as BrainLab Kolibri [27].These demonstrate the usefulness of robots in this application. The Neuromate robot has achieved a DBS spatial lead placement accuracy of 1.7mm in 51 patients, though other sources of error, including brain shift, led to sufficient anatomical accuracy in only 37 of the cases [28]. To date, there have been only a handful of attempts to develop MRI-compatible robotic systems for interventional procedures in closed-bore scanners (see [29] for an overview – some of them are shown in Figure 1.2), since the idea was first suggested in 1995 [30]. Subsequently, Chinzei et al. developed a general-purpose robotic assistant for open MRI that has been adapted for neurosurgery [29]. A more dexterous MRI-compatible system for neurosurgery is the neuroArm [31] as shown in Figure 1.3. However, none of these prior systems have been optimized for epilepsy treatment, and none have been design to insert a steerable, concentric-tube active cannula that can potentially compensate for observed but unmodeled sources of error during insertion.
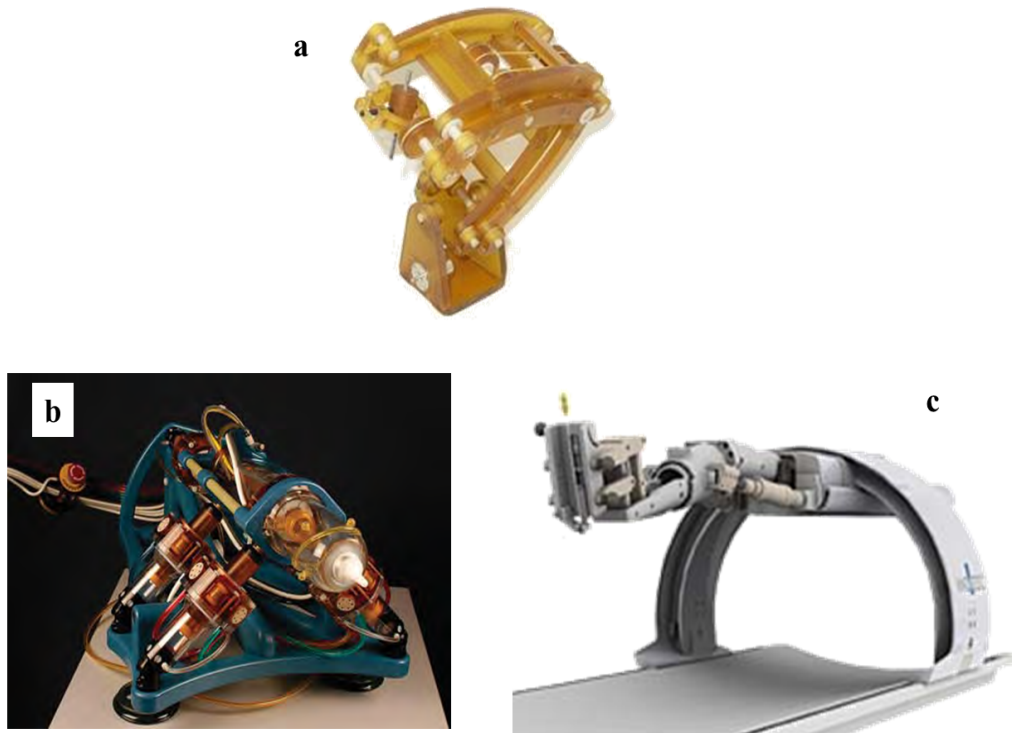
Figure 1.2: Some examples of prior MRI compatible robots. a) A robot designed for neural interventions in a MRI that is actuated by piezoelectric motors by WPI [32]. b) Pneumatic MRI compatible prostate brachytherapy robot developed at Johns Hopkins [33]. c) Pneumatic InnoMotion robot by Innomedic GmbH, Herxheim, Germany [29].
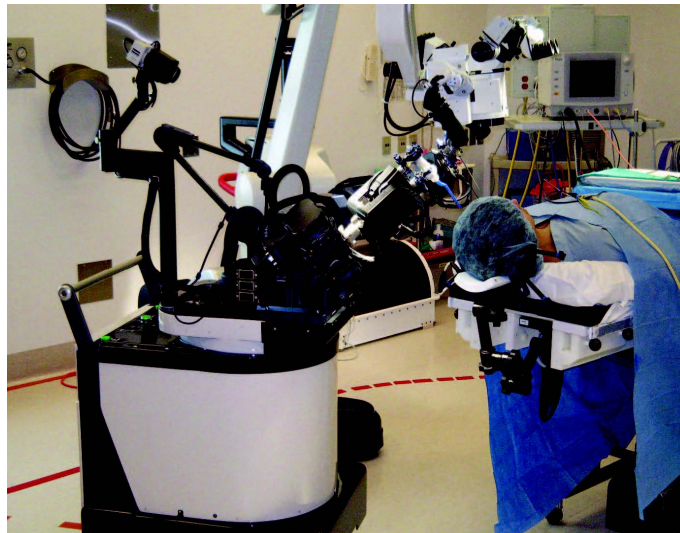
Figure 1.3: The NeuroArm manipulator developed by MDA space robotic engineers, of CanadArm fame, and University of Calgary [29].

1.2 Thesis Contributions

The proposed system is a unique integration of state of the art conformal therapeutic ultrasound, MRI-compatible robotic control and MRI tracking and monitoring technologies to solve a critical clinical problem that has never before been approached with ablative therapy. The system is designed to enable highly accurate interventional ablation tool localization and steering, and ablation volume shaping for treating a desired, and potentially geometrically complex, volume in the brain. While our primary interest in this project is epilepsy, we also note that in addition to the brain, this technology has application in multiple other organ sites (i.e lung and kidney). Our MRI-compatible robotic system will incorporate automation into the planning and execution of needle placement procedures. It will improve the accuracy and reproducibility with which ablation tool may be delivered and manipulated. Its ability to synchronously perform the surgical intervention and obtain images seem likely to enable unprecedented control of the delivery of therapeutic interventions. The proposed work will advance the state of the art in conformal ablative therapy and MRI-guided robotics. The use of synchronous automation and real-time MRI-based anatomical and thermal feedback will provide the necessary improvements in accuracy, conformal therapy shaping, and real-time dose monitoring to overcome the obstacles which have impeded use of MRI guidance in robotics and thermal ablation in neurosurgery. The specific contributions of work presented here for complete ablation of the hippocampus comprises:

- Design, modeling, and analysis of the overall epilepsy treatment system

- Design and fabrication of a novel robotic mechanism

- Confirmation of MRI compatibility of various materials and components

- Tuning and experimental evaluation of a pneumatic controller developed by Comber and Barth [34]

- Evaluation of targeting accuracy on the benchtop and in the scanner.

Chapter 2

Design Considerations and Requirements

2.1   Workspace Requirements

To characterize the available workspace for needle insertion to the hippocampus shown in Figure 2.1, a preoperative MR image was processed using the open-source DICOM viewer Osirix [35]. The workspace was segmented with assistance from a experienced neurosurgeon, the resulting volume in an average sized adult head is shown in Figure 2.4. To easily access the back of the head, the best position for the patient is facing down or facing up with the chin close to the chest as in Figure 2.2, but clinical viability has to be yet determined by an anesthesiologist to ensure that the position is not interfering with proper breathing of the patient. The positioning of the robot with a head-coil has to be evaluated in case better image quality is needed, but a vast variety of head-coil designs are available providing position flexibility for the robot. The distance between the insertion point and the hippocampus is approximately 100mm and the zone available for insertion is about 1200mm^2 shown on Figure 2.3. Concentric tubes can be specially custom designed to fit this specific application with the ability of rotate and translate telescopically. The cannula must be able to navigate from the insertion point to the hippocampus. Toward satisfying these requirements, the robot includes two prismatic motions and one rotational motion, as described on
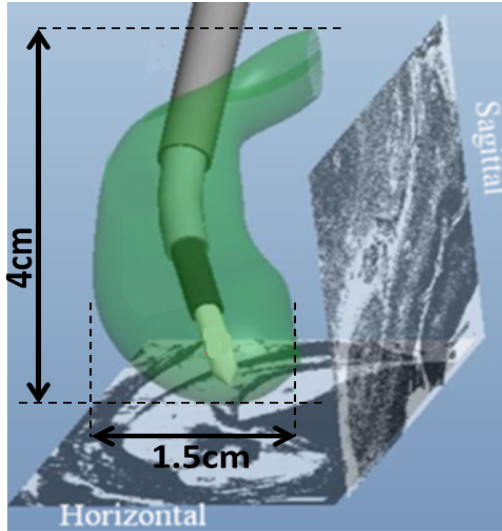
Figure 2.1: Workspace for needle insertion to the hippocampus with approximate dimensions.

Table 2.1.

Degree of Freedom	Linear	Linear	Rotation
Maximum Motion	150mm	150mm	360 °
Actuation	Pneumatic	Manual	Pneumatic

Table 2.1: Kinematic description of the robot.

The robot has to operate in a constrained space between the patient's head and the scanner bore which is typically less than 60cm in diameter, implying that an average space of 20cm is available for the robot if it must be positioned between the patient and the scanner shown in Figure 2.5.
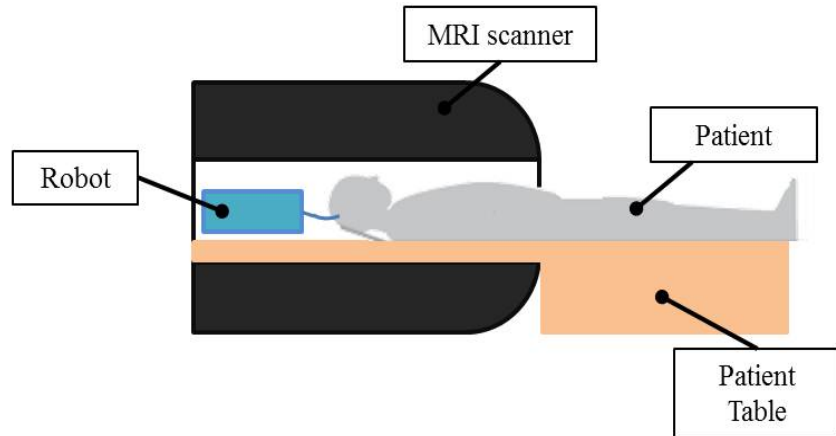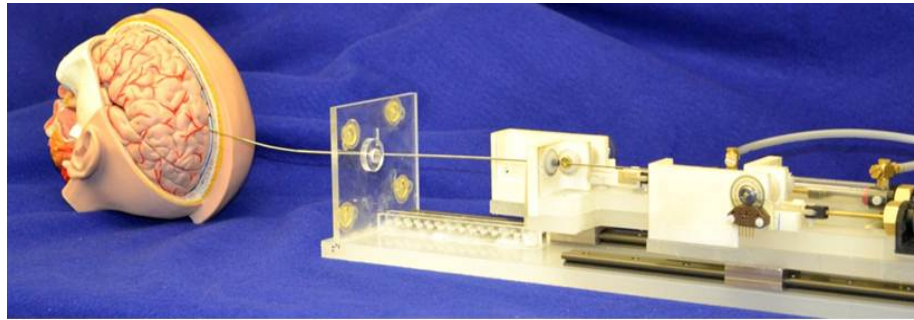
Figure 2.2: Patient positioning for needle insertion.
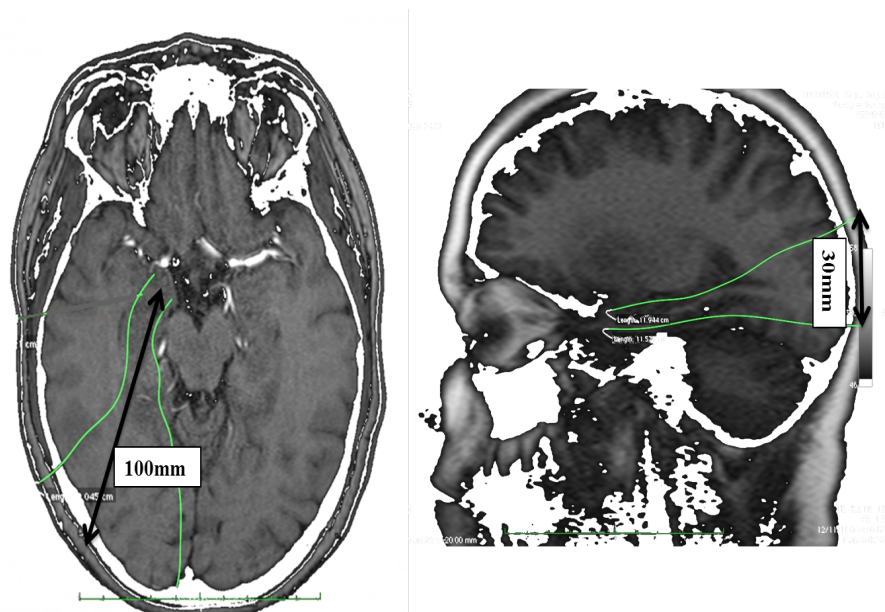
Figure 2.3: Brain MRI with delimited insertion workspace and approximate dimensions.
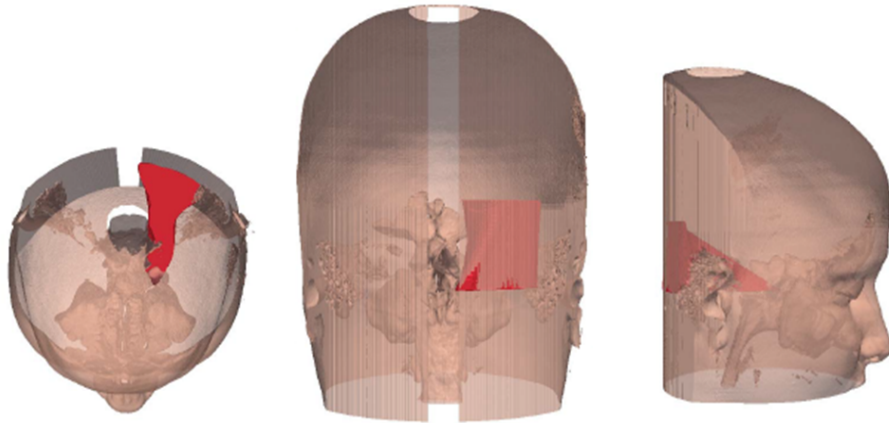
Figure 2.4: Workspace available in an adult head.

Figure 2.5: Space available in the MRI bore to place the robot.

2.2 MRI Requirements

The system has to operate inside the bore of high-field of 1.5T or 3T MRI scanner, which are commonly used in patients. Therefore, the traditional actuators and sensors cannot be used, and ferromagnetic materials must be also avoided because they represent a high risk being excessively heated or acting as projectiles. Non-ferromagnetic materials can be used, but they can produce artifacts and heating in the images due to the induced eddy currents. According to ASTM Standard F2052 [36] the MR safety is described as:

- MRI safe: The device, when used in the MR environment, has been demonstrated to present no additional risk to the patient or other individual, but may affect the quality of the diagnostic information. The MR conditions in which the device was tested should be specified in conjunction with the term MR safe since a device that is safe under one set of conditions may not be found to be so under more extreme MR conditions.

- MRI compatible: A device is considered MRI compatible if it is MRI safe and if it, when used in the MRI environment, has been demonstrated to neither significantly affect the quality of the diagnostic information nor have its operations affected by the MR device. The MR conditions in which the device was tested should be specified in conjunction with the term MR compatible since a device that is safe under one set of conditions may not be found to be so under more extreme MR conditions.

2.3   Discussion

As previously stated the design challenges of a MRI compatible robot arise from the high magnetic fields (1.5T or 3T) and the limited space in the scanner (approximately a maximum of 20cm in height above the patient). Additionally, the active cannula must be able to navigate from the insertion point to the hippocampus in a limited space, delimited by critical structures of the brain. These imply the need to address the dimensionality, safety and MRI compatibility of the system. Therefore, a compact robot design fabricated with MRI-compatible materials that drives an active cannula capable of navigating through the constrained workspace in the brain is needed.

Chapter 3

Initial Feasibility Study with a

Piezoelectric-Actuated Robot

To asses the targeting accuracy of an active cannula inside an MRI machine, a study with an existing piezoelectric-actuated robot [37] was conducted in collaboration with the Automation and Interventional Medicine (AIM) Robotics Laboratory at Worcester Polytechnic Institute. From this study [38] we conclude that it is possible to accurately reach image-space targets with an active cannula inside a MRI scanner with an MRI compatible robot. Some aspects of the material in this chapter were completed solely by WPI personnel, including the robot design (aside from attaching the curved tubes), and the fiducial design and evaluation. Notice that the system shown in Figure 3.1 is intended as an experimental setup, and further improvements including use of exclusively sterilizable materials need to be made before it can be used in human cases.

3.1 System Concept and Architecture

We adapt the needle placement robot described in [37] such that the robot supports control of three concentric tubes. The robot is MRI-compatible and resides inside the MRI scanner bore during a procedure. The MRI robot controller, adapted from [39],
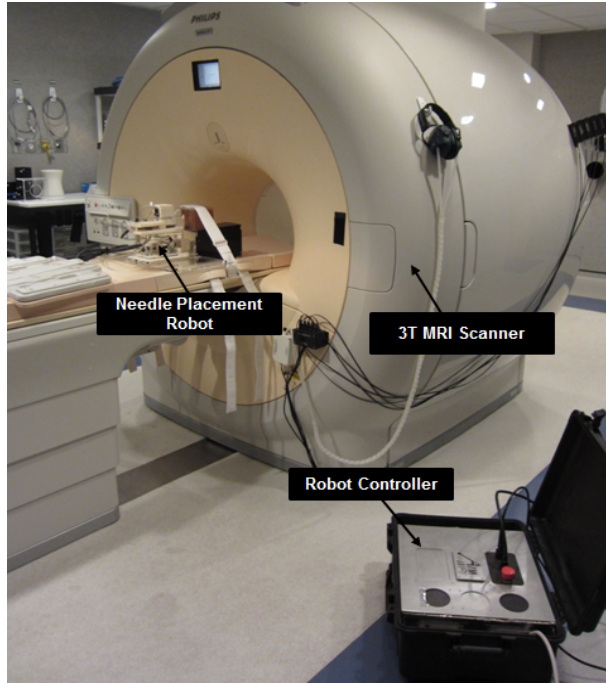
Figure 3.1: System configuration with robot and controller in the MRI scanner room.

resides inside the MRI scanner room beside the scanner bed as shown in Figure 3.1. The system is controlled from a workstation outside the scanner room connected via a fiber optic communication link to the robot controller. On the workstation is the modular robot control software shown in Figure 3.2, which can be used to directly control the robot or interface with a navigation system such as 3D Slicer over OpenIGTLink [40]. This software incorporates registration between the robot and MR image space such that a specific location in the MR image volume can be targeted. Inside this software, we can incorporate the forward and inverse kinematics for the robot.
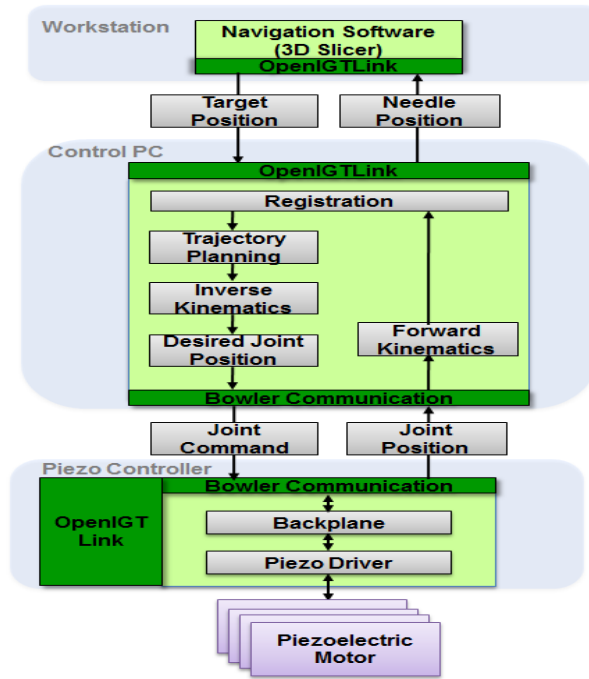
Figure 3.2: System architecture for control of the robot.

3.2 Multi-Slice Fiducial Registration

The robot is registered to the patient coordinate system, referred to as image-space coordinates, based on imaging a fiducial frame attached to the robot as shown in Figure 3.3. The fiducial frame attached to the robot is made of seven tubes filled with high contrast fluid and configured in a set of Z shapes in three orthogonal planes [41]. A new approach is utilized wherein multiple slices of the frame are used together to determine the 6-DOF position and orientation of the frame on the robot with respect to the scanner. Figure 3.6 illustrates one T2-weighted fast spin echo image of the cannula. The registration algorithm first segments the image and compensates for the irregular shape of the fiducial to find the best fitting ellipse. The seven points from
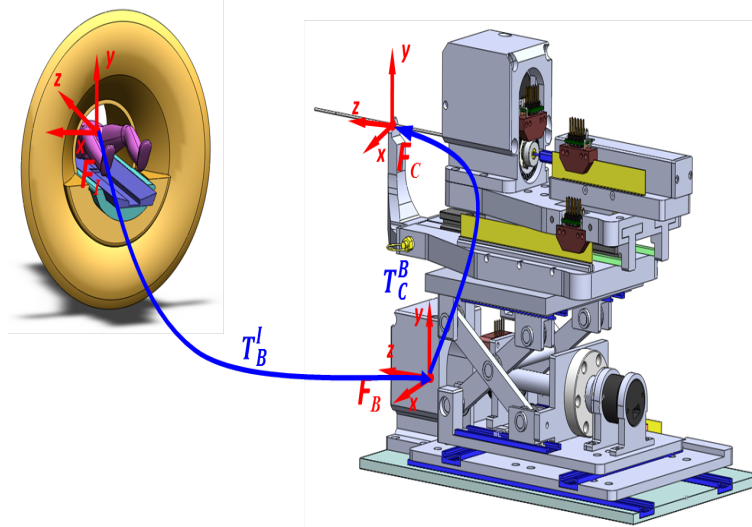
Figure 3.3: Coordinate frames of the robotic system for registration of the robot to MR image space (i.e. patient coordinates) and determining the required active cannula inverse kinematics.

several slices are then utilized to calculate the 6-DOF position and orientation of the robot with respect to the scanner origin. An independent evaluation of registration accuracy in the MRI scanner showed sub-pixel resolution with a mean error of 0.27mm in translation and 0.16° in orientation; the corresponding RMS error is 0.33mm and 0.46°. The corresponding series of homogeneous transformations is used to determine the continuum robot's tip location in cannula frame :

$$p_C = T_C^B T_B^I p_I$$

where p_C is the desired point expressed in the cannula frame, T_C^B is the transformation between the robot base frame and the cannula frame (i.e. the frame at the base of the cannula, where it exits the rest of the robot), T_B^I is the transformation between the robot base frame in the image frame, and p_I. In the navigation software, a desired p_I is selected from the MR image volume. This desired position p_I is sent to the robot control interface software from the planning workstation which uses inverse kinematics

to calculate the required joint positions which are transmitted to the robot controller to drive piezoelectric actuators.

3.3   Accuracy Assessment in MRI Phantom Trials

The accuracy of the robot-cannula system was evaluated by active cannula steering under MR imaging. The phantom tissue used for the experiments was simulated muscle ballistic test media (Corbin, Inc., USA). This soft, rubber-like material was molded into a 10 x 10 x 15cm rectangular phantom. The phantom was then placed inside a head coil, and the robot was initialized to a home position in front of the phantom as shown in Figure 3.4. 44 image slices of the phantom are acquired inside a 3 Tesla Philips Achieva scanner.
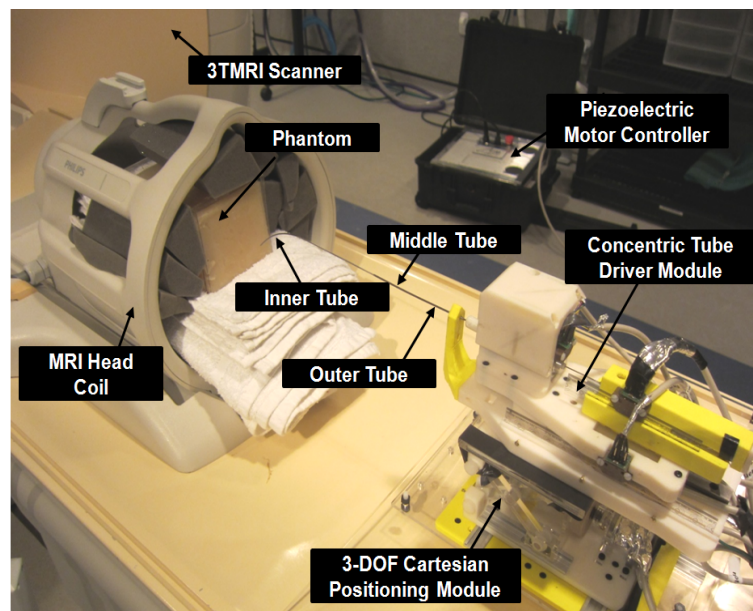
Figure 3.4: The Active cannula manipulation robot configured for phantom trials inside a 3T MRI scanner. The piezoelectric motor controller is also shown inside scanner room.

A diagnostic imaging T2-weighted fast spin echo protocol (repetition time 2700ms, echo time 22ms, slice thickness 2mm and 0.5mm x 0.5mm pixel size) was used to visualize the needle insertion trajectory.

Three trajectories were evaluated in the phantom in the MRI as shown in Figure 3.5. The following procedure ensures that the active cannula follows the desired trajectory (i.e. the shaft follows the tip exactly) as it is inserted into the phantom: the motion begins with all three tubes such that their tips are at the entry point into the phantom and the rotation of the middle tube set to the desired angle, then all three tubes move forward together a distance $\ell_1+\ell_2$, then the outer tube is stopped and the inner two tubes translate simultaneously a distance ℓ_3, and finally the middle tube is stopped and the innermost tube is extended a distance ℓ_4 (see section 5.1.1 and Figure 5.2 for an illustration of these distances). In this experiment, the three trajectories correspond to a translation of the middle tube (Tube 2) of 45mm at rotation angles of 0°, 90°, and 180°. Figure 3.6 shows the MR image volume for one of the curved trajectories. In this image, the 44 axial slices are compounded into a 3D volume which is re-sliced into the three planes shown. In each set of MR images, the 3D trajectory of the inserted cannula is measured by determining the location of the corresponding signal void in each slice. Figure 3.5 shows results from the three robotic active cannula insertion trials overlaid with the inverse kinematic theoretical model from 5.1. Blue dots represent the measured tip position from the acquired MR image volume. The three cylindrical curves represent the theoretical trajectory based on the kinematic model. The theoretical tip position and MRI needle void position are shown in Table 3.1. The Cartesian errors of the three trajectories are: 1.21mm,

20
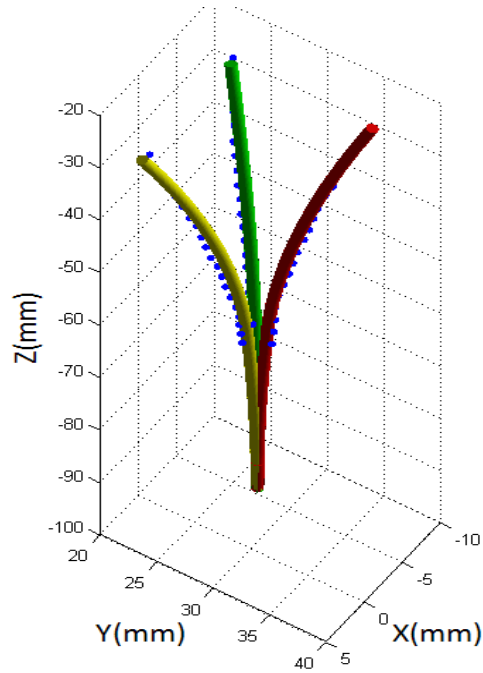
Figure 3.5: Results from three robotic active cannula insertion trials inside the MRI scanner. Blue dots represent the measured tip position from the acquired MR image volume. Red, Green, and Yellow curves represent the theoretical trajectory based on the kinematic model.

0.61mm and 2.24mm.

3.4   Conclusion

The accuracy of a MR image-guided concentric tube continuum robotic system with piezoelectric actuation was studied. The robot provides motion with joint-level precision better than 0.03mm. The MRI compatibility, task space accuracy and MRI-guided needle placement were evaluated to validate the system's targeting ability in image-guided surgery. RMS error in free space of active cannula placement was 1.00mm and three trajectories executed inside MRI showed an accuracy of 0.61 - 2.24mm. The errors present are due to sensor error (MRI needle void identification
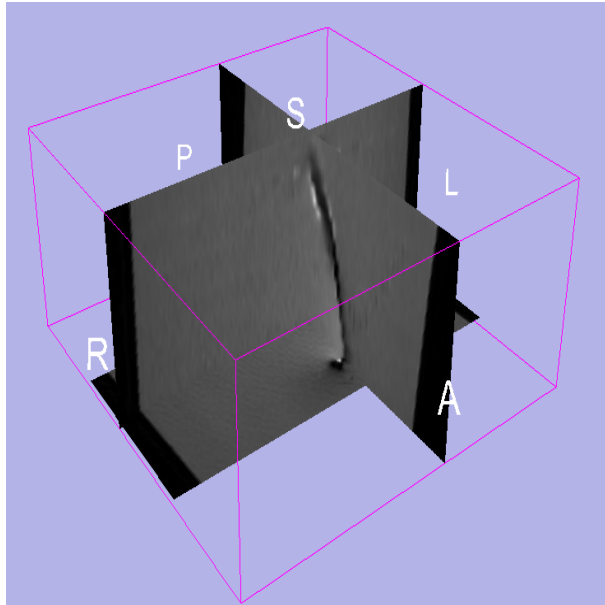
Figure 3.6: Volumetric MRI showing a representative active cannula path inserted into a phantom by the robot inside the MRI scanner. The needle is inserted along the L-S direction (vertical in this figure) and is shown in the sagittal plane along with two additional cross-sectional planes.

and imaging resolution), manipulator positioning error, calibration error, and un-modeled frictional forces and tissue interaction forces on the active cannula. These errors will be addressed through the use of image-guided closed-loop control, which we anticipate being capable of compensating for all of them.

	Model (*mm*)	MRI Data (*mm*)	Tip Error (*mm*)
Red	x: -8.35 y: 35.18 z: -26.49	x: -7.14 y: 35.23 z: -26.48	1.21
Yellow	x: 4.06 y: 23.61 z: -26.25	x: 3.52 y: 23.27 z: -26.40	0.61
Green	x: -8.35 y: 23.20 z: -26.49	x: -7.36 y: 23.41 z: -24.40	2.24

Table 3.1: Actual and Theoretical Tip Positions.

Chapter 4

Mechanical Design

As described in Chapter 1, there had been limited development on MRI compatible robots, and none of them has been specifically design to enable ablation of a complex volume in the brain. The design of a novel robot, the actuator and position sensor selection, the controller hardware and the materials selection are the subject of this chapter.

4.1 Design Overview

The robot consists of a modular 3 DOF cannula driver. The cannula driver provides 2-DOF (rotation and translation) of the pre-curved middle tube (Tube 2) and 1-DOF translation of the straight outer tube (Tube 3) that simulates the ablator, the outer tube (Tube 1) is fixed on the front plate, see Figure 5.2 for an illustration of the tubes. The rotational stages are actuated by a cylinder that moves a rack and pinion system, which is coupled with a bevel gear creating a 90° transmission. The orientation of the needle is the same as the orientation of the pistons achieving a small footprint to meet the space constraints discussed on Section 2.1. The translation stage carries the rotation module that was describe previously by attaching the piston to the needle carrier, which is mounted on a low-friction aluminum rail. The system is pneumatically actuated to avoid image artifacts produced by other types of actuators.
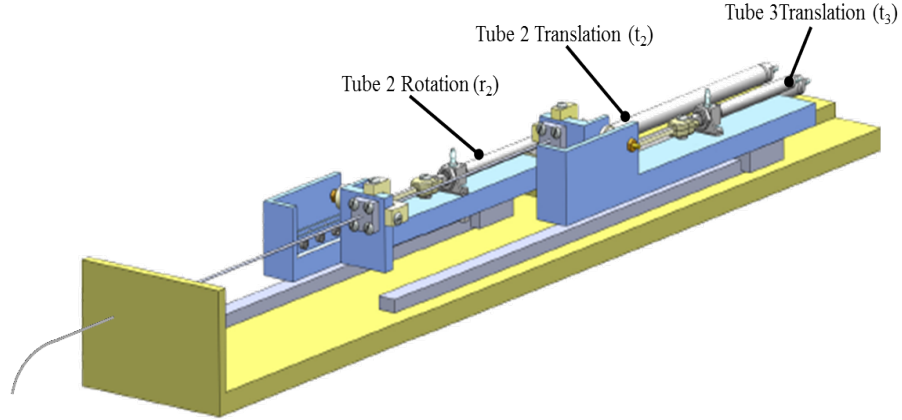
Figure 4.1: An illustration of the DOF and actuation placement for the MRI compatible robot where r_2 represents the rotation of the second tube, t_2 is the translation of the second tube.

Optical encoders were used to sense position because of their small effect on image quality. Pressure sensors and proportional valves were located 5m from the scanner for MRI safety and compatibility. A CAD model of the design is shown in Figure 4.1, which is compact (820mm x 130mm x 85mm) system, and resulted in a prototype made from MRI-Compatible materials as shown in Figure 4.2.

4.2 Actuator Selection

The magnetic field restricts our choice of actuators because the materials used in traditional robots are not suitable for high magnetic field environments. Furthermore, the constraints for developing a MRI compatible robot to assist during surgery include the ability to take images in real time with high quality, meaning that robot materials and electronics cannot distort the images. Our choice of actuators is based on previous studies [42] where two piezoelectric motors and a pneumatic cylinder are
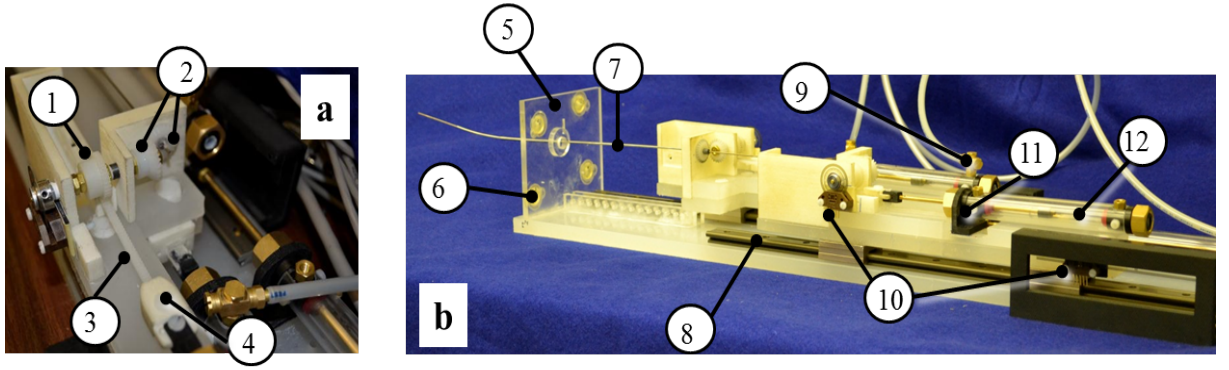
Figure 4.2: The MRI compatible robot. (a) A top view of the front module of the robot showing 1) Nylon spur gear 2) Nylon bevel gear 3) Nylon rack 4) ABS coupling rack/cylinder. (b) A side view of the whole robot showing 5) Acrylic front plate 6) Fiducials 7) Active Cannula 8) Aluminum Linear rail 9) Brass Fitting 10) Encoder 11) ABS cylinder base 12) MRI Compatible pneumatic cylinder.

compared in an experiment where the signal-to-noise ratio (SNR) of MRI images is measured under different conditions. Figure 4.4 shows the signal degradation presented with different actuators. The conclusion that can be drawn from this study is that pneumatic cylinders do not have negative impact on the SNR, where SNR is described by the signal intensity in the center of the phantom divided by the noise intensity in the periphery. Signal intensity is defined as the mean pixel intensity in the region of interest (ROI). Noise intensity is defined as the root mean square (RMS) signal intensity in an ROI outside of the phantom. The pneumatic cylinder (Figure 4.5) is designed specially for MR compatibility and low friction (0.01N) by Airpot (Airpel, Model E9 Non-Magnetic) with a borosilicate glass cylinder, a carbon graphite piston, and a brass rod. The cylinders can handle up to 100psi, and can apply forces up to 46.8N, but due to force requirements and dynamics we only require a maximum pressure of 35psi for this particular application. Directly actuated proportional directional control valves from Festo (MPYE-5-M5-010-B) were selected
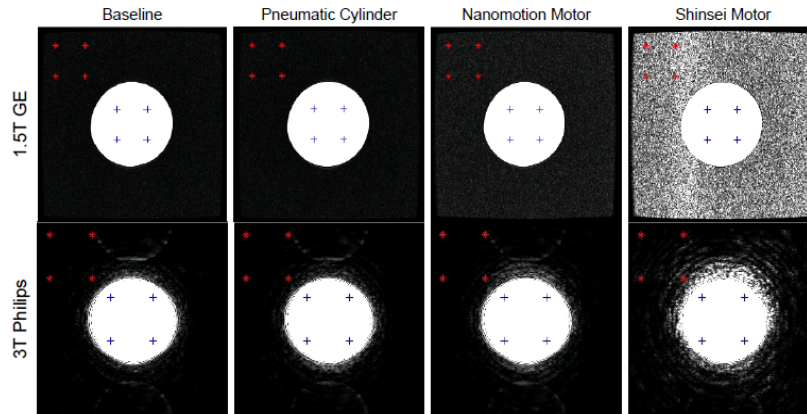
Figure 4.3: Representative results showing the difference in images obtained between baseline and motor running conditions (reproduced from [42]).
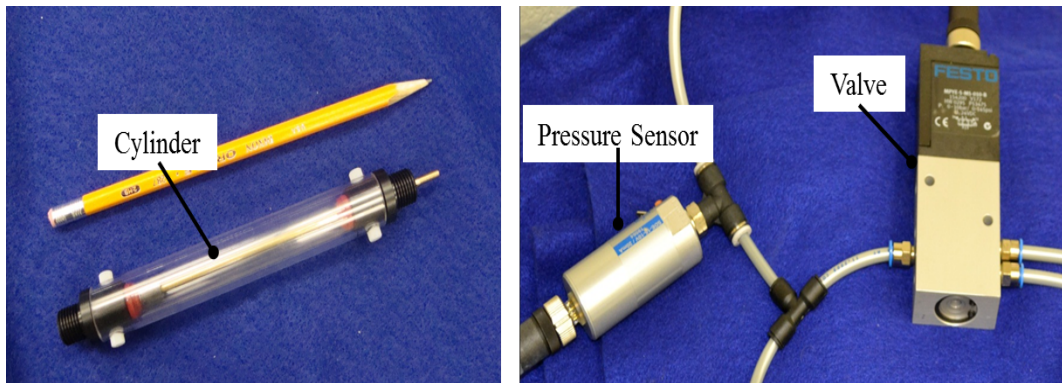
Figure 4.4: Proportional Directional Control Valve, Pressure Sensor and Cylinder.

because they enable control of the position of the spool. These valves are controlled by an analog voltage signal, and they provide a flow rate of 100 l/min. The pressure transmitter from Festo (SDET-22T-D10-G14-U-M12) provides the system with relative pressure measurements. The valves and pressure sensors are situated at the foot of the bed and are connected by 5m of tubing to the robot for safety in the MRI room.
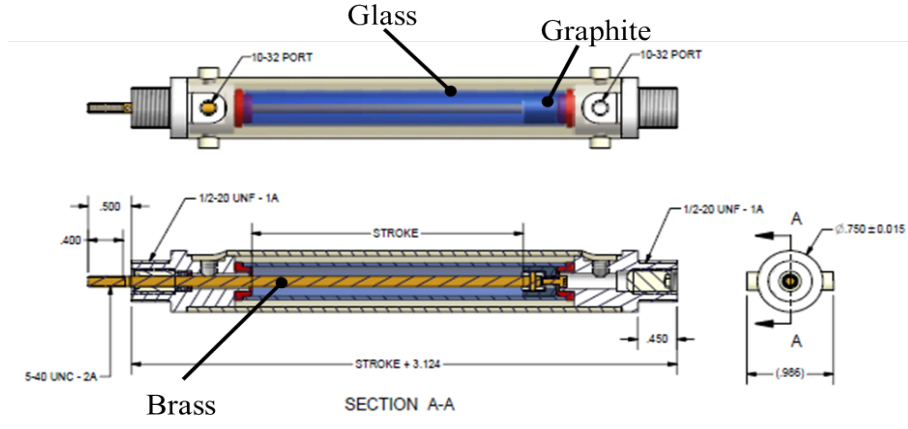
Figure 4.5: Schematic of the MRI compatible cylinder with materials.

4.3   Position Sensing

Sensing options such as linear potentiometers, magnetic sensors or cameras are not practical for MRI environment. Incremental optical encoders from US Digital (EM1-1250 rotary and EM1-500 linear) were selected for this robot based on results on [43]. They consist of a LED source and a detector enclosed in a small plastic package, and they are placed directly on the robot by attachment to an aluminum shaft. This type of encoder performs well in the MRI environment as shown in Figure 4.6 and described in [43].

4.4   MRI Material Compatibility

Safety of the patient and health care personnel requires avoidance of ferromagnetic materials, and experiments were conducted on the impact of non-ferromagnetic metals present on the robot, such as brass fittings and aluminum rails. Experiments have

Phantom Only   Encoder Present   Difference Image
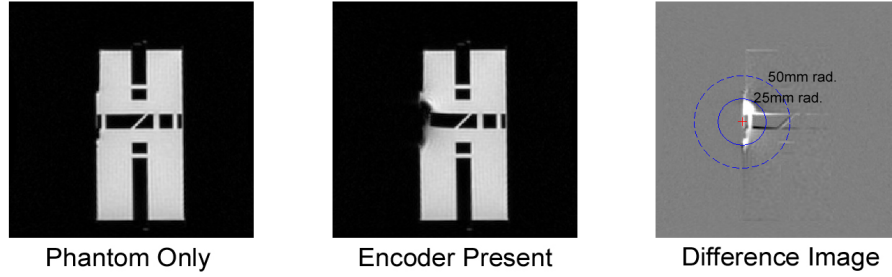
Figure 4.6: MRI compatibility evaluation of optical encoder in a 1.5T scanner (reproduced from [43]).

been conducted on a 3T Philips Achieva scanner obtaining an inconsequential rise in temperature over time when a series of images are taken within a time spacing of approximately 1minute/image as shown on Table 4.1. Here, the components were placed at the center of the scanner bore and a series of three images were taken. A high and fast increase of the temperature was observed when the components were placed at the wall of the scanner bore, but we are not concerned about this because our robot is not going to be attached to the scanner wall. Tests were performed to

	First Image	Second Image	Third Image
Fittings (brass)	19.25°C	19.45°C	19.95°C
Guide Block (aluminum)	19.65°C	19.80°C	20.30°C
Nut (brass)	20°C	20.45°C	20.60°C

Table 4.1: Temperature test with metallic materials with a room temperature of 19°C.

evaluate plastic materials (FLEX, ABS) to MR compatibility to ensure image quality. A 3T Philips Achieva MRI scanner was used, and plastic specimens were attached to the surface of phantom (Magnaphan EMR051) Figure 4.7. The material tensile specimens were placed on the left side of the phantom which was positioned on a
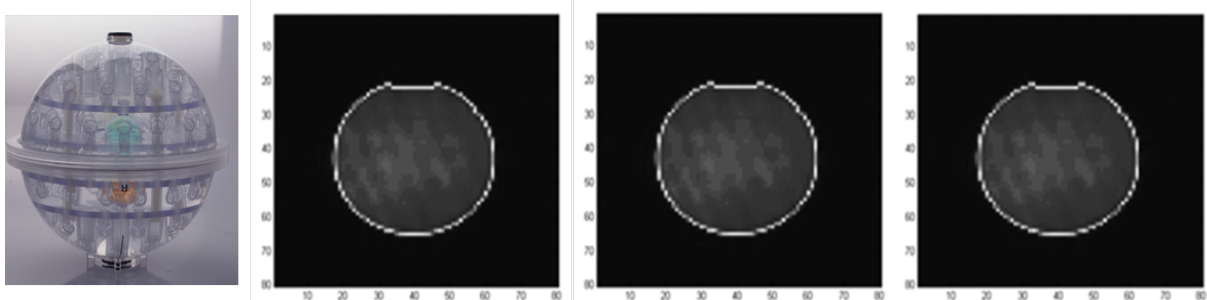
Figure 4.7: MRI compatibility evaluation for plastic materials in a 3T MRI. From left to right: Phantom, MRI Phantom baseline, MRI Phantom with FLEX, MRI Phantom with ABS. No artifacts were detected from the plastics.

head coil in the middle of the MRI scanner.

4.5 Robot Controller Hardware

The MRI is very sensitive to electrical signals. For this reason, all the electrical connections were made with twisted pair shielded cables. The robot controller (valves and pressure sensors) were placed inside the scanner room 5m from the scanner bed as shown in Figure 4.8. The target and host computers are located in the control room. They run Matlab XPC real-time Target at 1kHz with a multifunctional data acquisition board (NI PCI–6229) with analog outputs and inputs to read pressure sensor signals and to send commands to the valves. A counter board with eight channels (Contec CNT32–8M(PCI)) is used to read the incremental encoders.

Figure 4.8: Diagram representing computer and pneumatic connections.

Once the actuators, position sensing, and electronic hardware previously discussed were assembled. The materials and individual components used proved not to distort the MR images or create hazards for health care personnel or patients. We were ready to address the control structure of the system, which is explained on Chapter 5.

Chapter 5

Modeling and Control

A controller for driving the active cannula to a desired location was implemented and is shown in Figure 5.1. In order to achieve an specific position (x, y, z) the controller needs to coordinate the three DOF (r_2, t_3, t_2). This coordination is made by the inverse kinematics explained in Section 5.1. Section 5.2 explains the pneumatic piston-cylinder modeling which is later integrated in Section 5.3 with Sliding Mode Control.
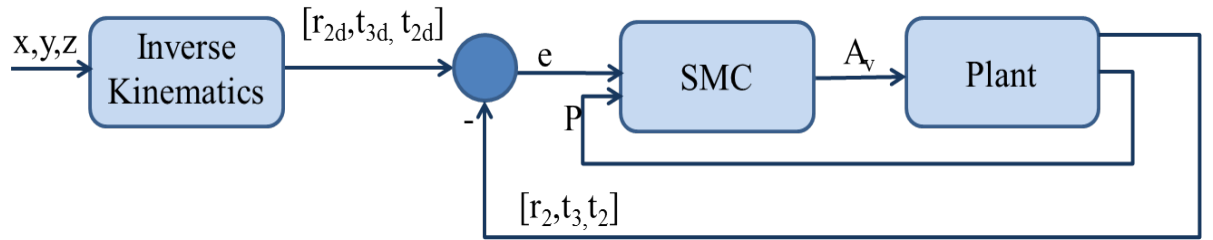
Figure 5.1: Structure of the control.

5.1   Active Canula Kinematics

Our prototype active cannula uses two concentric Nitinol tubes, with an inner Nitinol wire representing a simulated ablator or biopsy needle. These are assigned numbers from largest to smallest, with index 1 indicating the outer tube (see diagram in Figure 5.2). The outer tube and inner wire are straight, while the middle tube has a pre-
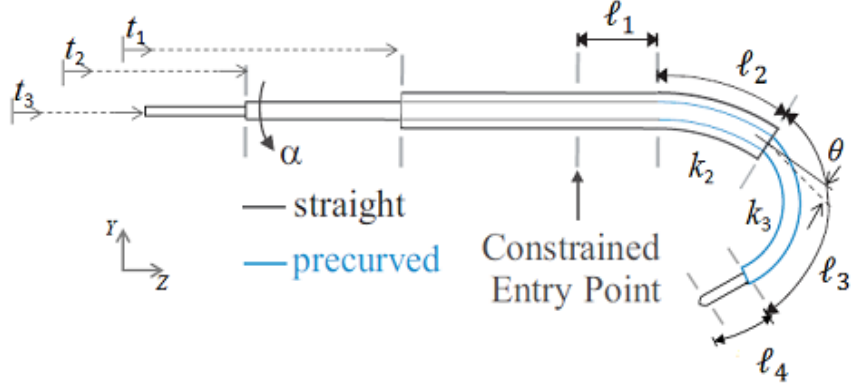
Figure 5.2: Illustration of the 3-part concentric tube continuum manipulator shown with the variables used for the active cannula kinematics.

curved section at its tip with a constant curvature κ of $0.0054mm^{-1}$. Although the innermost element is a flexible wire, for simplicity of exposition we will simply refer to all three of these concentric elements as "tubes".

5.1.1 Forward Kinematics

The kinematic equations provided here are similar to those given in [44], with the minor modifications. The robot shape consists of four segments, each with a constant curvature. The curvatures k_2 and k_3 and the length of each of the segments ℓ_1, ℓ_2, ℓ_3, ℓ_4 are calculated from the actuated distances t_1, t_2 and t_3, which are the insertion distance of each tube's base from its starting point, as measured by the robot's encoders. The starting point (i.e. home position) is defined to be the distances t_1, t_2 and t_3 when the tip of each tube is at the Constrained Entry Point. Due to finite clearance between tubes, the middle tube (Tube 2) exits the outer tube (Tube 1) with an angular offset of θ. The lengths of the sections shown in Figure 5.2 are

given by,

$$\ell_1 = max(t_2 - L_C, 0)$$

$$\ell_2 = max(t_1 - \ell_1, 0)$$

$$\ell_3 = max(t_2 - \ell_2 - \ell_1, 0)$$

$$\ell_4 = max(t_3 - \ell_3 - \ell_2 - \ell_1, 0),$$

$$(5.1)$$

the curvatures of the overlapping sections are:

$$k_2 = \frac{E_2 I_2}{E_1 I_1 + E_2 I_2 + E_3 I_3} \kappa$$

$$k_3 = \frac{E_2 I_2}{E_2 I_2 + E_3 I_3} \kappa,$$

$$(5.2)$$

where E_i is the Young's Modulus of the ith tube and I_i is the cross sectional moment of inertia of tube, and L_C is the length of the pre-curved section of the middle tube (Tube 2). The forward kinematics then consists of the series of homogeneous transformations:

$$T_{tip} = T_\alpha T_1 T_2 T_\theta T_3 T_4,$$

$$(5.3)$$

where intermediate transformations are defined as:

$$T_\alpha = \begin{bmatrix} \cos\alpha & -\sin\alpha & 0 & 0 \\ \sin\alpha & \cos\alpha & 0 & 0 \\ 0 & 0 & 1 & 0 \\ 0 & 0 & 0 & 1 \end{bmatrix}$$

$$(5.4)$$

$$T_1 = \begin{bmatrix} 1 & 0 & 0 & 0 \\ 0 & 1 & 0 & 0 \\ 0 & 0 & 1 & \ell_1 \\ 0 & 0 & 0 & 1 \end{bmatrix}$$

$$(5.5)$$

34

$$
T_2 = \begin{bmatrix} 1 & 0 & 0 & 0 \\ 0 & \cos(k_2\ell_2) & -\sin(k_2\ell_2) & \frac{\cos(k_2\ell_2)-1}{k_2} \\ 0 & \sin(k_2\ell_2) & \cos(k_2\ell_2) & \frac{\sin(k_2\ell_2)}{k_2} \\ 0 & 0 & 0 & 1 \end{bmatrix} \tag{5.6}
$$

$$
T_\theta = \begin{bmatrix} 1 & 0 & 0 & 0 \\ 0 & \cos\theta & -\sin\theta & 0 \\ 0 & \sin\theta & \cos\theta & 0 \\ 0 & 0 & 0 & 1 \end{bmatrix} \tag{5.7}
$$

$$
T_3 = \begin{bmatrix} 1 & 0 & 0 & 0 \\ 0 & \cos(k_3 l_3) & -\sin(k_3\ell_3) & \frac{\cos(k_3\ell_3)-1}{k_3} \\ 0 & \sin(k_3 l_3) & \cos(k_3\ell_3) & \frac{\sin(k_3\ell_3)}{k_3} \\ 0 & 0 & 0 & 1 \end{bmatrix} \tag{5.8}
$$

$$
T_4 = \begin{bmatrix} 1 & 0 & 0 & 0 \\ 0 & 1 & 0 & 0 \\ 0 & 0 & 1 & \ell_4 \\ 0 & 0 & 0 & 1 \end{bmatrix} \tag{5.9}
$$

Thus, T_{tip} gives the position and orientation of the tip of the cannula as a function of the measured actuator configurations: t_1, t_2, t_3, and α.

5.1.2   Inverse Kinematics

To place the tip of the active cannula at a desired target, we must invert the forward kinematic mapping given in previous section. To do this, we performed a nonlinear

optimization using Matlab's *fminsearch* function. This enables us to determine the actuator values which minimize the difference between the kinematic model-predicted and desired tip positions. To provide the algorithm with an initial guess, we first sampled the cannula's configuration space using a uniform discretization of 100 actuator configurations, and computed the tip position at each configuration. We then used the configuration with the lowest tip distance to the desired target as our initial guess. In order to minimize tissue damage and have the cannula deploy in a follow the leader manner, the deployment sequence starts by rotating the middle curve tube, flowing by its axial translation and ending with the inner tube translation.

5.2 Pneumatic Piston-Cylinder Modeling

A mathematical model of a pneumatic actuator has been well described in [45], [46] and in the following subsections (5.2.1, 5.2.2, 5.2.3) we summarize results. A schematic representation of the pneumatic actuator system is shown in Figure 5.3, it includes the pneumatic cylinder, valves and pressure and position sensors.
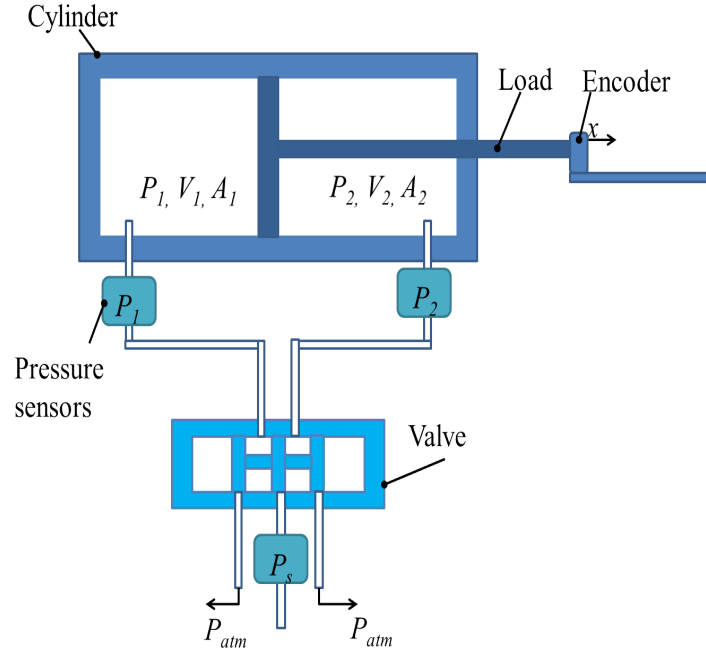
Figure 5.3: Schematic of a pneumatic cylinder-valve system.

5.2.1 Piston-Load Dynamics

The equation of motion for the piston is:

$$M\ddot{x} = P_1 A_1 - P_2 A_2 - P_{atm} A_r - \beta\dot{x}, \tag{5.10}$$

where the area of the piston rod A_r is calculated as $A_1 - A_2$, β is the viscous friction coefficient, M is the mass of the load, piston and rod, P_1 and P_2 are the absolute pressures at both chambers, P_{atm} is the absolute atmospheric pressure. For simplicity Coulomb friction is neglected.

5.2.2 Chamber Model

Assuming and ideal gas and isothermal conditions (T=constant), the pressure dynamics given by Equation 5.11 where the first term represents the effect on mass in or out the chamber, and the second term accounts for piston motion

$$\dot{P}_i = \frac{RT}{V_i}\dot{m}_i - \frac{P_i\dot{V}_i}{V_i},$$ (5.11)

5.2.3 Valve Model

The valve is the control element of the system, and is in charge of letting the air flow in and out of the piston chambers. If the upstream to downstream pressure ratio is larger than a critical value P_{cr}, we will have choked flow. If the pressure ratio is smaller than P_{cr}, we will have unchoked flow. The equation for both cases is

$$\begin{cases} \dot{m}_v = C_f A_v C_1 \frac{P_u}{\sqrt{T}} \text{ if } \frac{P_d}{P_u} > P_{cr} \\ \dot{m}_v = C_f A_v C_2 \frac{P_u}{\sqrt{T}} \left(P_d P_u\right)^{\frac{1}{k}} \sqrt{1 - \left(\frac{P_d}{P_u}\right)^{\frac{k-1}{k}}} \text{ if } \frac{P_d}{P_u} \leq P_{cr} \end{cases}$$ (5.12)

where $\dot{m}_v$ is the mass flow through valve orifice, C_f is a nondimensional discharge coefficient, P_u and P_d are upstream and downstream pressure respectively and,

$$C_1 = \sqrt{\frac{k}{R}\left(\frac{2}{k+1}\right)^{\frac{k+1}{k-1}}}$$ (5.13)

$$C_2 = \sqrt{\frac{2k}{R(k-1)}}$$ (5.14)

$$P_{cr} = \left(\frac{2}{k+1}\right)^{\frac{k}{k-1}}.$$ (5.15)

For air ($k = 1.4$)

In order to relate the pneumatic piston-cylinder modeling equations with area of the

valve (A_v) which is going to be the output of the controller, we take the derivative of 5.10 and substitute $\dot{P}_i$ into 5.11 to finally substitute $\dot{m}_v$ into equation 5.13.

5.3 Precision Position Tracking using Sliding Mode Control

This section contains work done by Comber and Barth, and is included for completeness, for further reference see [34]. In order to overcome unknown parameters of our plant such as friction and to properly address the compressibility of air, a Sliding Mode Controller was implemented. The sliding surface is defined so that if the state trajectory is on the sliding surface ($s = 0$), the error will tend to zero. The sliding surface chosen is

$$s = \left(\frac{d}{dt} + \lambda\right)^{n-1} \int e. \tag{5.16}$$

with $n = 3$ because relationship between piston and chamber dynamics is given by the first derivative of Equation 5.10, which is a third order system.

Expanding Equation 5.16 and taking its derivative, we obtain:

$$\dot{s} = \frac{1}{M}\left(\dot{P}_1 A_1 - \dot{P}_2 A_2 - \beta \ddot{x}\right) - \dddot{x_d} + 3\lambda \ddot{e} + 3\lambda^2 \dot{e} + \lambda^3 e. \tag{5.17}$$

To drive the states' trajectory onto a sliding surface we want s^2 to be a Lyapunov-like function given by,

$$\frac{1}{2}\frac{d}{dt}s^2 \leq -\eta|s|. \tag{5.18}$$

Using chain rule for differentiation of Equation 5.18 and substituting Equation 5.11 into Equation 5.17, we obtain the control law,

$$A_v = \frac{\dddot{x}_d - \frac{1}{M}\left(-\frac{P_1 A_1}{V_1}\dot{V}_1 + \frac{P_2 A_2}{V_2}\dot{V}_2 - \beta\ddot{x}\right) - 3\lambda\ddot{e} - 3\lambda^2\dot{e} - \lambda^3 e - \eta sgn(s)}{\frac{RT}{M}\left(\frac{\dot{m}_1}{V_1} + \frac{\dot{m}_2}{V_2}\right)}. \qquad (5.19)$$

5.3.1 Control Tuning

This controller was adapted to the needs of our specific robot and the adjusted parameters can be seen at Table 5.1, where the mass corresponds to the load that each cylinder has to move (i.e. rack and pinion system, principal carriage) and β is the estimate of the viscous friction. In the case of λ, it has been observed that there is a great sensitivity of this parameter to the sealing of the cylinders and tubing. This parameter was evaluated for different cylinders in Table 5.1. Tuning was accomplished with real–time XPC target, which allows one to change the parameters of the controller at the same time that data is received for analysis. Therefore, λ was adjusted in real time while the controller was trying to follow a commanded trajectory. The goal was to achieve accuracy using a step response with minimal overshoot and chatter.

Parameter	Rotational	Translational
Mass (kg)	0.04	0.23
Stroke Length (mm)	80	150
$\beta(\frac{N}{m/s})$	15	7

Table 5.1: Sliding Mode Control Tuning Parameters.

Actuator	Tubing Length (m)	Pressure Supply (psi)	$\eta(\frac{m}{s^3})$	λ (Hz)
Rotational	0.15m	35	2	102
Translational	0.15m	35	2	60
Rotational	5m	35	2	120
Translational	5m	35	2	90

Table 5.2: Sliding Mode Control Tuning Parameters.

Chapter 6

Experimental Validation Studies

The pneumatic control accuracy of the system was evaluated using long (5m) and short (0.15m), commanding steps and sine waves. For this set of experiments the cannula tip was in free space. Accuracy was evaluated in benchtop experiments with a magnetic tracker. To test the robot MRI compatibility, a 3T MRI scanner was used.

6.1 Pneumatic Control Accuracy

Positioning accuracy is dependent on the servo pneumatic control system. The control algorithm for pneumatic servo control is based upon Sliding Mode Control (SMC) explained in Section 5.3. Bench-top experiments were done to study the precision of the actuators.

6.1.1 Short Pneumatic Lines

Experiments with short pneumatic tubing of 15cm long from the pressure sensors to the cylinder chambers were performed as an initial approach to ensure acceptable model following. Sinusoidal and step signals were commanded to the actuator in charge of rotational motion of the needle and the actuator in charge of transla-tional stage. It was observed that the commanded signal was closely followed with

an error close to 0.05mm. It is observed that the signal presents overshoot of approximately 1mm on the square trajectory due to unmodeled effects such as Coulomb friction.However, this is not a concern for our application ,because we will never ask our robot to react to such large step changes, instead specifying very small setpoint changes along a desired trajectory, as in Comber [34]. Tuning was necessary to be able to follow the commanded trajectory as shown in Table 5.2. We note that it remains to be defined how large setpoint steps can be (along with necessary control gains) such that we can guarantee lack of overshoot, but that if we are willing to sacrifice some tracking performance, it is possible to reach desired setpoints slower, without overshoot, as was done in [34]. Here, we tuned gains with tracking accuracy in mind, without regard to small overshoot.
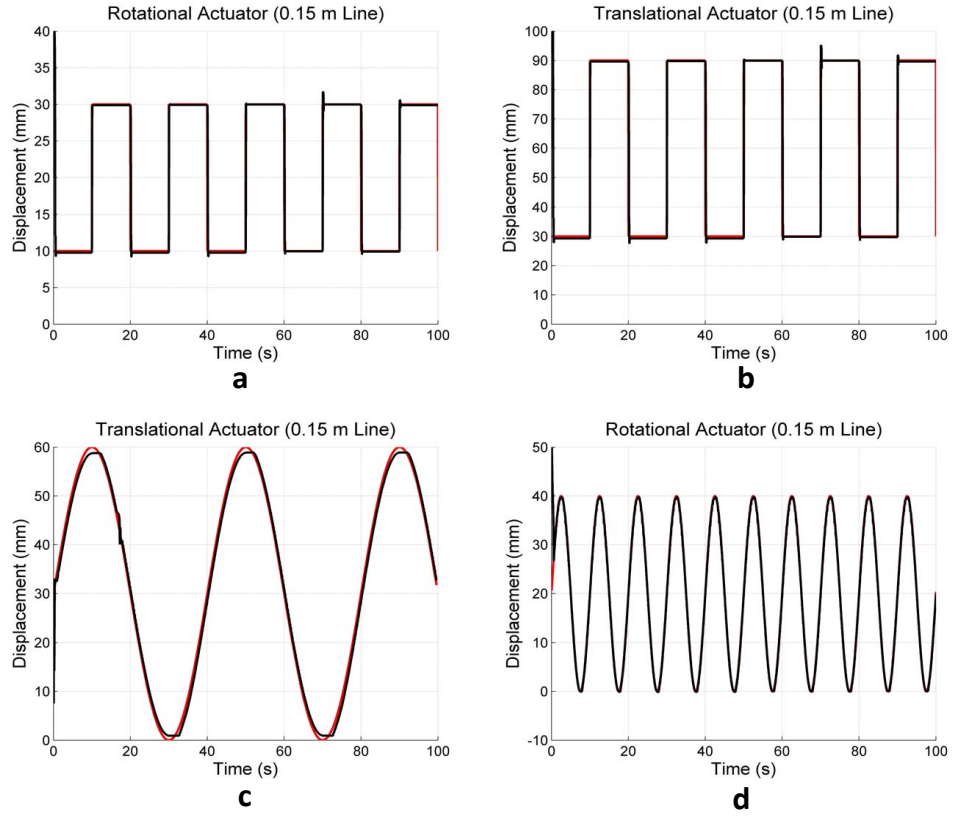
Figure 6.1: Command and Response Signals for 0.15m Line a) 0.05Hz, 30mm amplitude step signal for the rotational actuator b) 0.05Hz, 60mm amplitude step signal for the translational actuator c) 0.025Hz, 30mm amplitude sine wave for the translational actuator d) 0.1Hz, 20mm amplitude sine wave for the rotational actuator.

6.1.2 Long Pneumatic Lines

Experiments with long pneumatic tubing of 5m from the pressure sensors to the cylinder chambers were performed to fulfill the requirements of locating controller a safe distance from the scanner. A sinusoidal signal commanded to the actuators. Different control gains were necessary to be able to follow the commanded trajectory. Values used are shown on Table 5.2. Previous work by Yang et al. [47] addressing the problem of long transmission lines by modeling them as a time delay. Here, we

do not need to adopt this approach, because speed is not critical , instead choosing to shape our desired input trajectory such that changes are relatively slow and the system does not go unstable. To explore this for one specific example trajectory we created a curve by filtering a step.

Rotational Actuator (5 m Line)

Translational Actuator (5 m Line)
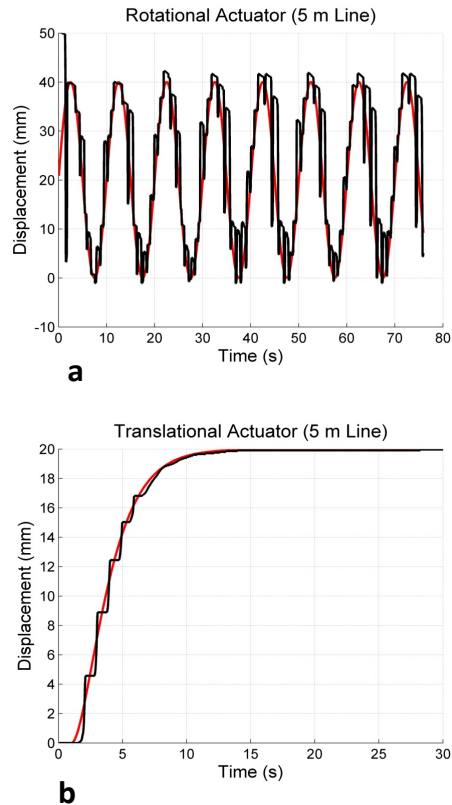
Figure 6.2: Command and Response Signals for 5m Line a)0.1Hz, 20mm amplitude sine wave for the rotational actuator. b)An arbitrary slowly changing desired trajectory constructed by filtering a 20mm step with a low pass filter.

6.2   Cannula Tip Free-Space Accuracy

Figure 6.3 shows the configuration of the robot and the magnetic tracker and their respective coordinate systems. It was necessary to do a point–based registration [48] to
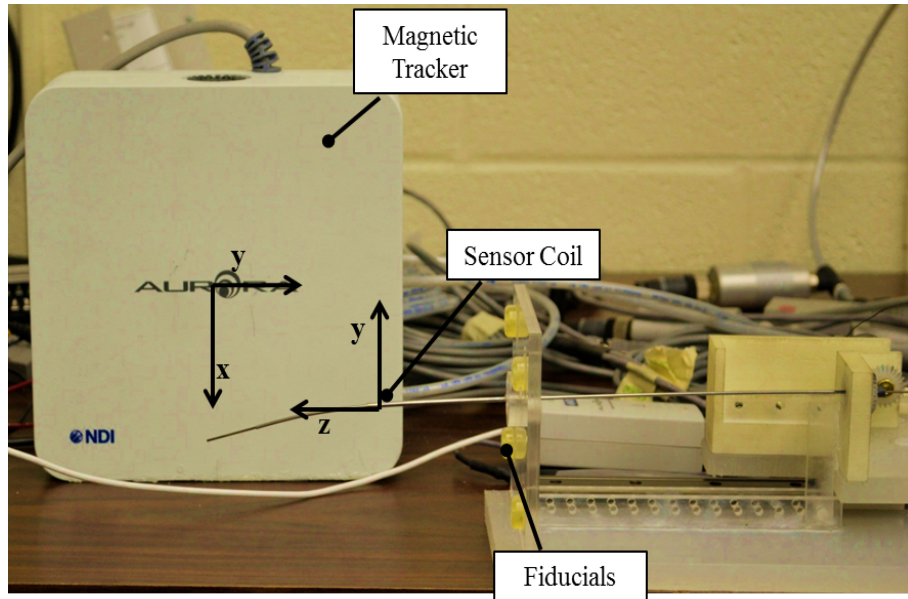
Figure 6.3: Experiment Set up with Magnetic Tracker.

align the points obtained with the Magnetic Tracker to the robot coordinate frame. The results are presented on Table 6.1. A minimum error of 5.42mm and maximum error of 6.25mm was registered, these errors are consequence of different factors including actuation control errors, kinematic model approximations (i.e. linear elasticity, unmodeled friction, uncertainty in measuring section curvatures, and magnetic tracker accuracy). However, we suspect that error from imprecisely done registration, as well as magnetic distortions may be the most significant sources of error, since average tip errors of less than 3mm (i.e. approximately 1.5-3% of arc length) have been previously achieved in experiments with concentric tube robots.

Kinematic Model (mm)	Error (mm)
x: -11.5 y: -11.5 z: 98.54	x: 4.90 y: 0.30 z: 3.36
x: -11.5 y: 11.5 z: 98.54	x: 0.10 y: 5.10 z: 1.86
x: 11.5 y: 11.5 z: 98.54	x: 4.90 y: 0.20 z: 2.56
x: 11.5 y: -11.5 z: 98.54	x: 0.86 y: 5.20 z: 3.36

Table 6.1: Theoretical Tip Positions and errors from a Magnetic Tracker experiment.

6.3 MRI Compatibility Experiments

Figure 4.8 shows the configuration of the hardware in the MRI room as it was placed for this experiment. The MR image in Figure 6.4 shows that there is no observable distortion or major artifacts on the images when the robot was actuated with pressure
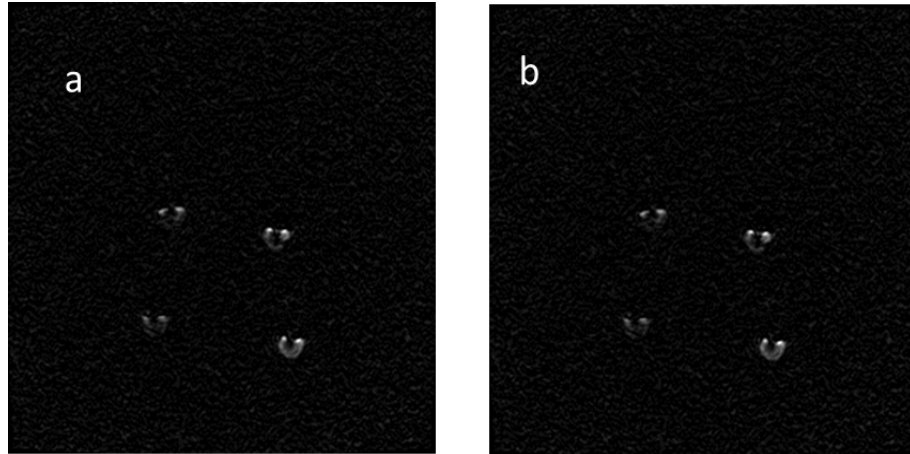
Figure 6.4: a) Baseline b) Image while operating the pressure sensors and the valves.

sensors and valves powered on. The fiducials shown in the figure are Gadolinium based contrast (Beekley – PinPoint).

6.4 MRI Cannula Tip Accuracy

Data on the tip of the needle in the MRI scanner was collected see Figure 6.5. The set up of the experiment is the same as in Section 6.3, and a series of needle tip desired final positions were commanded to the controller. MR images of the tip of the cannula and the fiducial on the robot front plate were collected after the cylinders were controlled to achieve the desired final position. Image processing to determine accuracy was done off-line with point-base registration. The results of the experiment are presented on Table 6.2 where the minimum error of the tip of the needle was 3.32mm and the maximum error was 4.45mm. These errors are due to the image resolution, the fiducial localization error, control accuracy and random errors. Information about the imaging work volume setting are presented in Table 6.3.

Figure 6.5: MRI-compatible robot in the 3T Philips Achieva scanner.

Kinematic Model (mm)	Error (mm)
x: 7.06 y: -7.06 z: 69.20	x: 0.87 y: 3.48 z: 2.65
x: 8.45 y: 8.45 z: 79.01	x: 0.12 y: 2.89 z: 1.64
x: -9.82 y: 9.82 z: 88.81	x: 3.89 y: 3.46 z: 1.29

Table 6.2: Theoretical Tip Positions and errors from a MRI experiment.

49

Parameter	Value
Foot-head length	240mm
Right-Left length	180mm
Slice thickness	5mm
Slice spacing	1mm

Table 6.3: Philips 3T Achieva work volume settings.

6.5 Discussion

A Sliding Mode Controller was implemented on a novel MRI-compatible robot, and different trajectory following experiments were performed with long and short pneumatic lines, achieving accuracy of 0.05mm on the actuators at the final position. The experiments presented in Section 6.1 were intended to show the accuracy that can be achieved with the pneumatic controller, but it was observed that perfect following of a the step trajectory presented overshoot, which is undesirable. Therefore, since neurosurgery does not require high speed of insertion, but rather excellent accuracy; we reach the final position by constructing a slowly changing desired trajectory (in our example, this was constructed from a filtered step). We suspect that there will be some upper bound on how fast and far setpoints may change such that stability is maintained and overshoot precluded, but establishing these is an area for future work.

Benchtop experiment with a Magnetic Tracker were performed and a minimum error of 5.42mm and maximum error of 6.25mm was registered, MRI experiments were performed showing 3.32mm minimum error and 4.48mm maximum error of the tip of the needle and no distortion was observed in the MR images when the controller was used.

Chapter 7

Conclusions

This dissertation has presented a new approach for needle steering as a interventional device for MRI–guided surgery. It was demonstrated that the robot is MRI compatible and that the sensors and actuators can operate under high magnetic fields without distorting the images, and individual material tests were performed under MR imaging to confirm the suitability of the robot components in this environment. The controller was successfully implemented for long transmission lines appropriate for the typical MRI scanner room disposition. The controller was implemented in Matlab XPC-Target to run in real time. Finally, a clinical application that takes advantages of the MRI technology, the minimum invasiveness of the active cannula and the ablation therapies was identified.

We foresee this type of system facilitating neurological procedures and reducing long-term health care costs associated with chronic management of epilepsy, and increasing the safety and quality of life for those who suffer from it. The surgeon using our system will be able to accomplish "point–and–click" surgery, indicating the location on the MRI image where he/she wishes the tip of the cannula placed.

Bibliography

[1] N. Garga and D. H. Lowenstein, "Posttraumatic epilepsy: A major problem in desperate need of major advances," *Epilepsy Currents*, vol. 6, no. 1, pp. 1–5, 2006.

[2] M. P. Earnest, G. E. Thomas, R. A. Eden, and K. F. Hossack, "The sudden unexplained death syndrome in epilepsy: Demographic, clinical, and postmortem features," *Epilepsia*, vol. 33, no. 2, pp. 310–316, 1992.

[3] P. De Flon, E. Kumlien, C. Reuterwall, and P. Mattsson, "Empirical evidence of underutilization of referrals for epilepsy surgery evaluation," *European Journal of Neurology*, vol. 17, no. 4, pp. 619–625, 2010.

[4] J. Engel, "Surgery for seizures," *New England Journal of Medicine*, vol. 334, no. 10, pp. 647–653, 1996.

[5] M. R. Sperling, "Sudden unexplained death in epilepsy," *Epilepsy Currents*, vol. 1, pp. 21–23, 2001.

[6] G. Jackson, A. Connelly, J. Duncan, R. Grunewald, and D. Gadian, "Detection of hippocampal pathology in intractable partial epilepsy: increased sensitivity with quantitative magnetic resonance t2 relaxometry.," *Neurology*, vol. 43, no. 9, pp. 1793–9, 1993.

[7] J. E. Leestma, J. F. Annegers, M. J. Brodie, S. Brown, P. Schraeder, D. Siscovick, B. B. Wannamaker, P. S. Tennis, M. A. Cierpial, and N. L. Earl, "Sudden

unexplained death in epilepsy: Observations from a large clinical development program," *Epilepsia*, vol. 38, no. 1, pp. 47–55, 1997.

[8] S. Lhatoo, J. Solomon, A. McEvoy, N. Kitchen, S. Shorvon, and J. Sander, "A prospective study of the requirement for and the provision of epilepsy surgery in the united kingdom.," *Epilepsia*, vol. 44, no. 5, pp. 673–6, 2003.

[9] J. I. Sirven, "The silent gap between epilepsy surgery evaluations and clinical practice guidelines," *European Journal of Neurology*, vol. 17, no. 4, pp. 522–523, 2010.

[10] W. T. Blume, A. G. Parrent, and M. Kaibara, "Stereotactic amygdalohippocampotomy and mesial temporal spikes," *Epilepsia*, vol. 38, no. 8, pp. 930 –936, 1997.

[11] H. F. Flanigin and B. S. Nashold, *Stereotactic lesions of the amygdala and hippocampus in epilepsy.*, vol. 23. Acta Neurochir, 1976.

[12] R. Heimburger, I. Small, J. Small, V. Milstein, and D. Moore, "Stereotactic amygdalotomy for convulsive and behavioral disorders," *Appl Neurophysiol*, vol. 41, no. 1-4, pp. 43–51, 1978.

[13] T. Hood, J. Siegfried, and H. Wieser, "The role of stereotactic amygdalotomy in the treatment of temporal lobe epilepsy associated with behavioral disorders," *Appl Neurophysiol*, vol. 46, no. 1-4, pp. 19 –25, 1983.

[14] T. Schmidt, R. Konig, M. Hlavac, G. Antoniadis, and C. R. Wirtz, "Lows and highs: 15 years of development in intraoperative magnetic resonance imaging,"

in *Intraoperative Imaging* (M. N. Pamir, V. Seifert, and T. Kiris, eds.), vol. 109 of *Acta Neurochirurgica Supplementum*, pp. 17–20, Springer Vienna, 2011.

[15] I. Chen, A. Coffey, S. Ding, P. Dumpuri, B. Dawant, R. Thompson, and M. Miga, "Intraoperative brain shift compensation: Accounting for dural septa," *IEEE Transactions on Biomedical Engineering*, vol. 58, no. 3, pp. 499–508, 2011.

[16] F. Jolesz, I.-F. Talos, R. B. Talos, IF snd Schwartz, R. Schwartz, H. Mamata, H. Mamata, D. F. Kacher, D. Kacher, K. Hynynen, K. Hynynen, N. McDannold, N. McDannold, P. Saivironporn, P. Saivironporn, L. Zao, and Z. L, "Intraoperative magnetic resonance imaging and magnetic resonance imaging-guided therapy for brain tumors.," 2002.

[17] F. A. Jolesz, *Interventional and intraoperative MRI: A general overview of the field*, vol. 8. Wiley Subscription Services, Inc., A Wiley Company, 1998.

[18] F. A. Jolesz and K. Hynynen, *Magnetic resonance image-guided focused ultrasound surgery.* Lippincott Williams & Wilkins, 2002.

[19] C. R. Weiss, S. G. Nour, and J. S. Lewin, "MR-guided biopsy: A review of current techniques and applications," *J. Magn. Reson. Imaging*, vol. 27, no. 2, pp. 311–325, 2008.

[20] W. A. Hall, H. Liu, R. E. Maxwell, and C. L. Truwit, "Influence of 1.5-tesla intraoperative MR imaging on surgical decision making: Intraoperative imaging in neurosurgery," 2003.

[21] P. Starr, J. Martin, Alastair, A. Martin, J. L. Ostrem, J. Ostrem, P. Talke, P. Talke, N. Levesque, N. Levesque, S. Larson, Paul, and L. PS, "Subthalamic nucleus deep brain stimulator placement using high-field interventional magnetic resonance imaging and a skull-mounted aiming device: technique and application accuracy.."

[22] D. F. Louw, T. Fielding, P. B. McBeth, D. Gregoris, P. Newhook, and G. R. Sutherland, "Surgical robotics: A review and neurosurgical prototype development," *Neurosurgery*, vol. 54, no. 3, pp. 525–537, 2004.

[23] T. Haidegger, L. Kovacs, G. Fordos, Z. Benyo, and P. Kazanzides, "Future trends in robotic neurosurgery: 14th nordic-baltic conference on biomedical engineering and medical physics," 2008.

[24] T. Varma, P. Eldridge, A. Forster, S. Fox, N. Fletcher, M. Steiger, P. Littlechild, P. Byrne, A. Sinnott, K. Tyler, and S. Flintham, "Use of the neuromate stereotactic robot in a frameless mode for movement disorder surgery," *Stereotact Funct Neurosurg*, vol. 80, no. 1-4, pp. 132–135, 2003.

[25] N. Tsekos, A. Khanicheh, A. Khanicheh, E. Christoforou, E. Christoforou, C. Mavroidis, and M. C, "Magnetic resonance compatible robotic and mechatronics systems for image guided interventions and rehabilitation a review study," *Annual Review of Biomedical Engineering*, vol. 9, pp. 351–387, 2007.

[26] H. Elhawary, Z. T. H. Tse, A. Hamed, M. Rea, B. L. Davies, and M. U. Lamperth,

"The case for MR-compatible robotics: a review of the state of the art," *Int. J. Med. Robotics Comput. Assist. Surg.*, vol. 4, no. 2, pp. 105–113, 2008.

[27] R. Pitto, S. Malak, and I. Anderson, "Accuracy of a computer-assisted navigation system in resurfacing hip arthroplasty," *International Orthopaedics*, vol. 33, pp. 391–395, 2009.

[28] K. Masamune, E. Kobayashi, Y. Masutani, M. Suzuki, T. Dohi, H. Iseki, and K. Takakura, "Development of an MRI-compatible needle insertion manipulator for stereotactic neurosurgery.," *J Image Guid Surg*, vol. 1, no. 4, pp. 242–8, 1995.

[29] K. Chinzei, N. Hata, F. Jolesz, and R. Kikinis, "MR compatible surgical assist robot: System integration and preliminary feasibility study: Medical image computing and computer-assisted intervention - miccai 2000," 2000.

[30] A. Boss, S. Clasen, M. Kuczyk, F. Schick, and P. Pereira, "Image-guided radiofrequency ablation of renal cell carcinoma," *European Radiology*, vol. 17, pp. 725–733, 2007.

[31] R. Gassert, E. Burdet, and K. Chinzei, "MRI-compatible robotics," *Engineering in Medicine and Biology Magazine, IEEE DOI - 10.1109 EMB.2007.910273*, vol. 27, no. 3, pp. 12–14, 2008.

[32] Y. Wang, G. Cole, H. Su, J. Pilitsis, and G. Fischer, "MRI compatibility evaluation of a piezoelectric actuator system for a neural interventional robot," in *Engineering in Medicine and Biology Society, 2009. EMBC 2009. Annual Interna-*

tional Conference of the IEEE DOI - 10.1109/IEMBS.2009.5334206, pp. 6072–6075, 2009.

[33] J. A. Cunha, I.-C. Hsu, J. Pouliot, M. Roach III, K. Shinohara, J. Kurhanewicz, G. Reed, and D. Stoianovici, "Toward adaptive stereotactic robotic brachytherapy for prostate cancer: Demonstration of an adaptive workflow incorporating inverse planning and an MR stealth robot," 2010.

[34] D. B. Comber and E. J. Barth, "Precision position tracking of MR-compatible pneumatic piston-cylinder using sliding mode control," in *Proc. DSCC and Bath. ASME Symp. Fluid Power and Motion Control*, 2011.

[35] A. Rosset, L. Spadola, and O. Ratib, "Osirix: An open-source software for navigating in multidimensional dicom images," 2004.

[36] "F2052-06e1 standard test method for measurement of magnetically induced displacement force on medical devices in the magnetic resonance environment."

[37] H. Su, M. Zervas, G. Cole, C. Furlong, and G. Fischer, "Real-time MRI-guided needle placement robot with integrated fiber optic force sensing," in *IEEE International Conference on Robotics and Automation (ICRA)*, pp. 1583 –1588, 2011.

[38] H. Su, D. Cardona, W. Shang, G. Cole, D. C. Rucker, R. Webster III, and G. Fischer, "A MRI-guided concentric tube continuum robot with piezoelectric actuation: A feasibility study." Accepted at: IEEE ICRA 2012 International Conference on Robotics and Automation, 2012 (In Press).

[39] G. Cole, K. Harrington, H. Su, A. Camilo, J. Pilitsis, and G. S. Fischer, "Closed-loop actuated surgical system utilizing in-situ real-time MRI guidance," in *International Symposium on Experimental Robotics - ISER 2010*, vol. 1, p. 1, 2010.

[40] J. Tokuda, G. S. Fischer, X. Papademetris, Z. Yaniv, L. Ibanez, P. Cheng, H. Liu, J. Blevins, J. Arata, A. J. Golby, T. Kapur, S. Pieper, E. C. Burdette, G. Fichtinger, C. M. Tempany, and N. Hata, "Openigtlink: an open network protocol for image-guided therapy environment," *Int. J. Med. Robotics Comput. Assist. Surg*, vol. 5, no. 4, pp. 423–434, 2009.

[41] G. Fischer, I. Iordachita, C. Csoma, J. Tokuda, S. DiMaio, C. Tempany, N. Hata, and G. Fichtinger, "MRI-compatible pneumatic robot for transperineal prostate needle placement," *Mechatronics, IEEE/ASME Transactions on*, vol. 13, no. 3, pp. 295 –305, 2008.

[42] G. Fischer, A. Krieger, I. Iordachita, C. Csoma, L. Whitcomb, and G. Fichtinger, *MRI Compatibility of Robot Actuation Techniques- A Comparative Study*, vol. 5242. Springer Berlin - Heidelberg, 2008.

[43] G. Fischer, *Enabling Technologies for MRI Guided Interventional Procedures*. PhD thesis, Johns Hopkins University, 2008.

[44] R. Lathrop, D. Rucker, and R. Webster III, "Guidance of a steerable cannula robot in soft tissue using preoperative imaging and conoscopic surface contour sensing," in *IEEE International Conference on Robotics and Automation*, pp. 5601–5606, 2010.

[45] D. McCloy and H. Martin, *Control of fluid power: analysis and design.* Ellis Horwood series in engineering science, E. Horwood, 1980.

[46] E. Richer and Y. Hurmuzlu, "A high performance pneumatic force actuator system: Part ii—nonlinear controller design," *Journal of Dynamic Systems, Measurement, and Control*, vol. 122, no. 3, pp. 426–434, 2000.

[47] B. Yang, U.-X. Tan, A. McMillan, R. Gullapalli, and J. Desai, "Design and control of a 1-dof MRI-compatible pneumatically actuated robot with long transmission lines," *Mechatronics, IEEE-ASME Transactions on*, vol. 16, no. 6, pp. 1040–1048, 2011.

[48] Sonka, Milan, and J. M. Fitzpatrick, *Medical Image Processing and Analysis*, vol. 2. Handbook of Medical Imaging, 2009.